Summer 8-3-2022

RAMAN THERMOMETRY OF GRAPHENE BASED THERMAL MATERIALS

Pengcheng Xu
paulx@smu.edu

RAMAN THERMOMETRY OF GRAPHENE BASED THERMAL MATERIALS

Approved by:

Prof. Kevin Brenner
Electrical and Computer Engineering
Thesis Committee Chairperson

Prof. Bruce Gnade
Mechanical Engineering

Prof. Prasanna Rangarajan
Electrical and Computer Engineering

Dr. Christo Bojkov
Physical Chemistry
Qorvo

RAMAN THERMOMETRY OF GRAPHENE BASED THERMAL MATERIALS

A Thesis Presented to the Graduate Faculty of the

Lyle School of Engineering

Southern Methodist University

in

Partial Fulfillment of the Requirements

for the degree of

Master of Science in Electrical Engineering

by

Pengcheng Xu

B.S., Electrical and Computer Engineering, University of Texas at Austin

August 3, 2022

ACKNOWLEDGMENTS

I would like to acknowledge my advisor Dr. Kevin Brenner. Despite the difficult time during the pandemic, he has made this work possible.

I would also like to acknowledge Jesus Alejandro Avendano Bolivar, for his contribution in the computational work presented in this thesis.

Xu, Pengcheng B.S., Electrical and Computer Engineering, University of Texas at Austin, 2020

Raman Thermometry of Graphene Based Thermal Materials

Advisor: Prof. Kevin Brenner

Master of Science in Electrical Engineering conferred August 3, 2022

Thesis completed August 3, 2022

With the growing demand for high performance computing, we are pushing for higher performance integrated circuits at an ever faster rate. Recent advances in semiconductor production technology sees transistors with a 5 nm process devices being produced for consumer use. This enabled engineers to pack tens of billions of transistors in a package no larger than a fingernail. However, that brings up a problem that we have been long battling against. How can we get rid of the heat produced by these billions of transistors. The current electronic performance is bottle-necked by the ability of the package taking heat away from the transistors. Traditional methods call for mounting the die onto metal using thermal paste or solder, which were good enough to conduct the heat for dissipation with previous technologies. But with the growing power density of modern integrated circuits, that can be problematic. Simply, packages made of metal do not take away the heat fast enough.

This thesis investigates thermal properties of graphene based materials. Using the method of Raman thermometry, we can observe the temperature of the materials whilst applying a heat flux at the same time. Using finite-element analysis, our computational model maps our experimental data and extracts the properties of the thermal interface and the material itself. Unlike conventional methods of measuring heat conductivity, raman thermometry is not as limited to the size and continuity of the material. This thesis will be looking at several materials that are difficult to characterize with conventional methods, by observing the temperature of the substrate and the thin film on top. It is also possible for us to calculate the thermal interface resistance. In this thesis, several graphene derived materials

will be investigated, such as graphene grown on metal foams, free standing graphene foams and graphene oxide papers. The results of the experiments show the thermal conductivity of the current graphene based foams can have a thermal conductivity of 630 W/mK for the solid portion of the graphene-metal foam structure, but 1.9 W/mK for the bulk material.

TABLE OF CONTENTS

LIST OF FIGURES

Figure Page

LIST OF TABLES

Table Page

To Mr. Francis Mikan for inspiring me to continue my work in science.

Chapter 1

Introduction

Power dissipation is perhaps the greatest challenge facing modern electron devices. The inability to dissipate their power per area, or heat flux (Q), has limited the performance of integrated circuits for nearly two decades [1]. It is also limiting the performance of discerete devices, such as radio-frequency (RF) GaN devices. Here, their power and frequency are limited by the temperature rise (ΔT), which is related to the heat flux by Fourier's law of $\Delta T = \frac{QL}{k}$ where L is the junction length and k is the thermal conductivity of the junction. This junction is typically formed with a thermal interface material (TIM) that mechanically, electrically, and thermally couples the device to the board. In this configuration, the thermal conductivity of the TIM directly impacts the device performance; the higher its thermal conductivity, the higher power or frequency the device can be operated at with an acceptable temperature rise. The problem that this thesis addresses is that today, state-of-the-art metallic TIMs have begun to approach the maximum thermal conductivity of what metals can provide, which limits our ability to increase the performance of RF devices. While industry has found short-term work arounds, like improving the RF signal efficiency using beam steering in 5G, a direct packaging solution that can limit temperature rise can have a major impact on a variety of civilian and military communication and radar systems.

In general, the thermal conductivity of a crystal is related to the mass of its atoms and strength of its chemical bonds. Crystalline forms of carbon, such as the sp [2] bonded graphite and sp [3] bonded diamond, have extremely high thermal conductivities due to their light atoms and strong bonds [2]. In fact, the highest known thermal conductivity (5,000 W/mK) was experimentally measured in a single layer of graphite [3], called graphene. This value for two-dimensional (2D) graphene is slightly higher than for three-dimensional (3D) graphite (or graphene supported on a substrate), which is thought to be on the order of 1,000 W/mK [4]. This discrepancy may arise from the damping of out-of-plane vibrations,

called flexural phonons, which contribute to the thermal conductivity [5] [6]. In contrast to the remarkable in-plane thermal conductivity of graphene/graphite, their out-of-plane conductivity is extremely low. Graphite is a layered material, whose strong in-plane bonding (5.9 eV) is contrasted by extremely weak out-of-plane forces (50 meV) holding the layers together. These forces arise from a nonbonded van der Waals (vdW) interaction [7]. As such, the anisotropy in the chemical bonding of graphite is reflected as a nearly three-fold anisotropy in its thermal conductivity [8]. These layered materials can have an out-of-plane thermal conductivity as low as 0.009 W/mK [9] [10], which is less conductive than air.

The introduction of graphite into metal or polymer composites holds tremendous promise for improving the thermal conductivity of TIMs. In this thesis, the term graphite will refer to both graphite and graphene, unless stated otherwise. There have been numerous attempts to integrate graphite with composites, however, their thermal conductivity is typically low and on the order of 10s of W/mK [11]. The reason for this is twofold, with both arising from the thermal anisotropy of graphite. The first reason is that the graphite must be continuous, otherwise the composite will reflect its poor out-of-plane thermal conductivity as heat must transport between material fragments. The second reason is that the graphite must be oriented in the direction of the power dissipation. Even if the graphite were continuous, if it was oriented parallel to the board, the device would be thermally insulated from the board rather than coupled to it. One method for fabrication graphite-metal composites is the direct chemical vapor deposition (CVD) of carbon onto the metal surface. These CVD methods are capable of producing extremely high-quality graphite layers [12] [13]. Furthermore, it is possible to apply CVD growth to arbitrary 3D metallic templates. For example, metallic foams can be graphitized to form continuous and oriented bulk materials [14].

In this thesis, we present methods for characterizing the thermal conductivity and material quality of graphite-metal foams for TIMs. Adopting work from porous materials [15], we demonstrate that Raman thermometry is capable of simultaneously characterizing the chemical disorder and thermal conductivity in graphite-metal composites. We find that the quality of the graphite, arising from the deposition process, clearly affects the thermal conductivity of the composite. We also demonstrate that, based on the volume fraction, the solid components of the composite can have thermal conductivities as high as 600 W/mK,

which is significantly higher than the best performing bulk metals (400 W/mK in Cu, Ag).

Chapter 2

Process Calibration

2.1 Overview

Raman thermometry is a new technique available after recent improvements on instrumentation and technology [15]. The high spectral resolution of the state-of-the-art Raman spectroscopy machines made measuring wavelength shifts down to one hundredth of a wavenumber possible. Since a fairly high power laser is used in a Raman spectroscopy system, the laser power absorbed by the sample during the measurement causes a temperature gradient in the sample. Because a Raman spectra measurement is taken at the same time, it is possible to measure the temperature at the same time. To make the data accurate, it is crucial to characterize the whole process.

2.2 Laser Power

The energy output is measured using a commercial laser power meter. The output of the laser is diffused onto a Si-based photo-diode sensor and read out directly [16]. A He-Ne Laser at 633 nm wavelength rated at 10 mW output power and a 532 nm fiber laser with 100 mW rated output power are installed in the Raman system. The Raman system controls the power output of the laser by making the laser pass through a series of neutral density filters. The system has 10 different power settings ranging from 0.01% to 100%. We need to characterize the linearity of the ND filters. Also, we need to measure the power output through different objectives. The power loss out of the objectives is significant enough to alter the result in the final device simulation. Figure 2.1 shows the results of the laser power calibration. There are major differences between the objectives of the system. This can be due to the difference in aperture of the objectives. Also, some power is lost within the optical path and from the lenses. Overall, the neutral density filters in the system are linear.

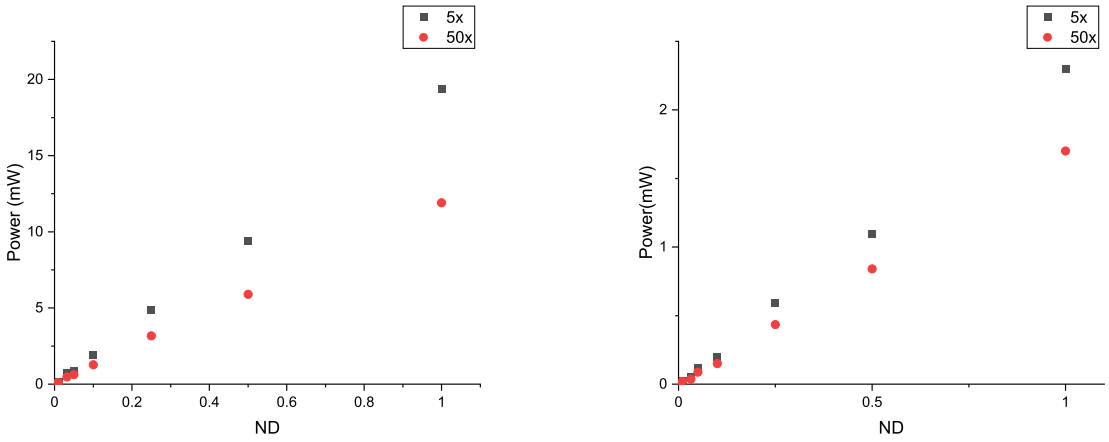

(a) 532 nm Laser Power Diagram

(b) 633 nm Laser Power Diagram

Figure 2.1: Laser power plot of the 2 lasers in Horiba LabRam system

2.3 Spot Size Calibration

The calibration of the spot size is done with a knife edge experiment. The laser is shown onto a metal pad with an edge created using lithographic and wet chemical methods. Figure 2.2 a) shows the basic setup of the experiment. The laser steps through the X and Z direction. The laser spot from the micro-raman system can be modeled as a Gaussian mode. The signal power of the TEM_{00} mode laser can be described by equation (2.1).

$$P(x) = P_0 \int_x^\infty \left(\frac{2}{\pi}\right)^{1/2} \frac{1}{\omega} \exp\left(\frac{-2x^2}{2}\right) dx \tag{2.1}$$

P_0 being the laser power, ω is the beam radius, and x is the direction the laser is traveling [17]. We can see that equation 2.1 is a version of the Gaussian error function (*erfc*). By collecting and characterizing the intensity of the Raman signal emitted from the substrate we can map the beam diameter of the laser spot at a given Z position. The intensity observed by the spectrometer follows the decay of the integrated Raman TEM_{00} mode following the complementary error function as the Raman signal gets covered by the metal deposited on top of the substrate.

The Horiba LabRam system used by our research group has a servo controlled Z axis. The knife edge experiment is repeated by stepping the laser beam through various points on

the X and Z axis. By fitting and extracting the radius from each pass through the deposited metal knife-edge, we can obtain the beam radius from each of the Z positions.

(a) Experimental setup

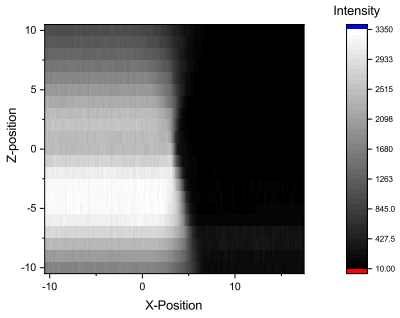

(b) Knife-edge experimental data

Figure 2.2: a) Experimental Setup, the laser beam in the illustration is shown onto the grey silicon substrate and across the deposited metal knife-edge. b) Knife-edge experimental data, plotted against X and Z axis. Visually we can see the focus is close to Z=0 μm but not exact. This is indicative of we cannot use one single point to determine the minimum spot size of the laser.

The intensity reading is indicative of the decay due to the *erfc* function. The beam radius at the focal plane is defined by equation 2.2 [18].

$$I \propto \exp\left(\frac{I^2}{r_0^2}\right) \tag{2.2}$$

The relationship between the observed intensity and the error function is defined by equation 2.3. [19].

$$A \propto erfc\left(\frac{x}{r_z}\right) \tag{2.3}$$

And the relationship between Z position and radius is defined by equation 2.4.

$$r = \sqrt{r_0^2 + a^2 z^2} \tag{2.4}$$

The measured radius is $\sqrt{2}/3S_{rad}$ where $S_{rad} = 3\sigma$ of the gaussian profile. From the exper-

imental data, we can obtain that the beam radius for this particular laser and objective is $S_{rad} = 950$ nm.

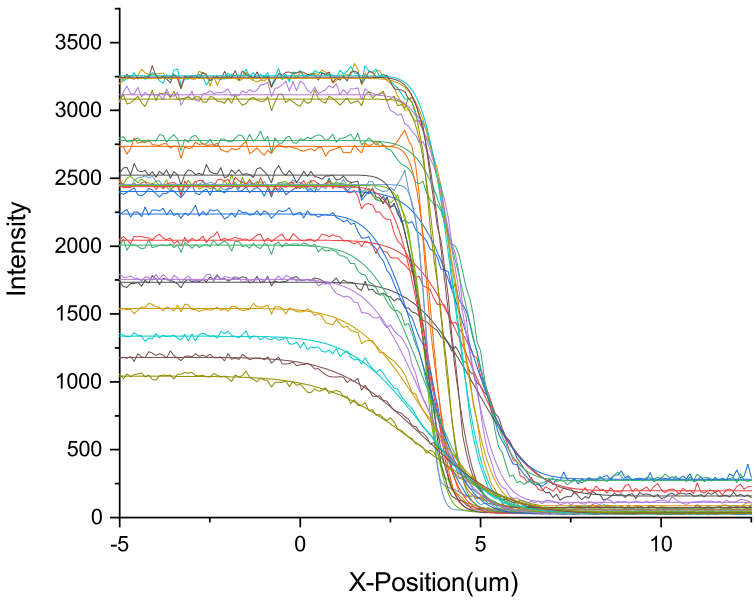

Figure 2.3: erfc fitted experimental data. *erfc* is a function of x position. r_z is extracted for each Z position

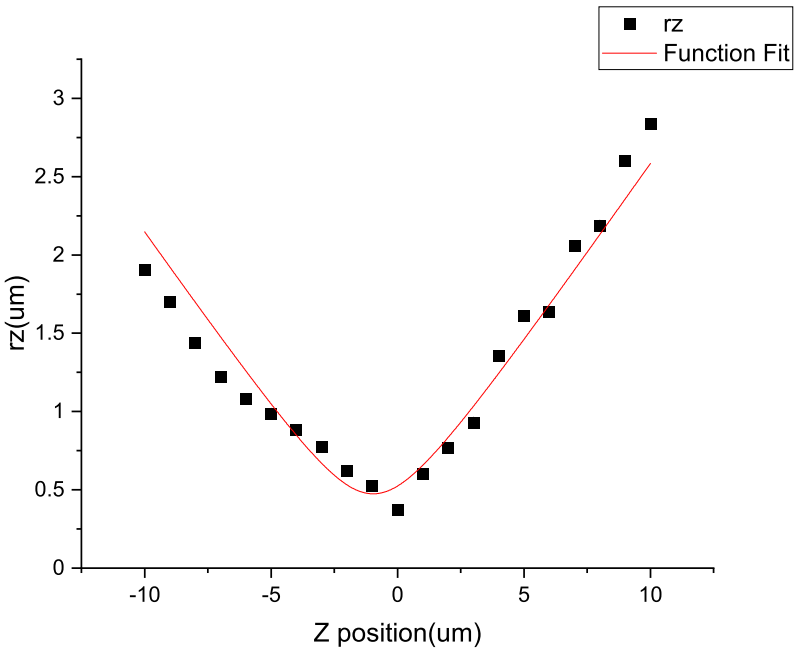

Figure 2.4: Fitted beam data, according to a Gaussian beam profile. r_0 is extracted at the focal plane.

2.4 Finite Element Analysis

The Finite Element Simulations were performed using the COMSOL Software. These simulations were tested using a variety of samples with different material stacks. The FEM offers us an opportunity to observe the behavior of each sample under different conditions, and compare the results with the experimental side of this work. The simulations took into consideration, the density (ρ), and heat capacity at constant pressure (Cp). Additionally, the beam was configured to spot radius of 1.25 nm and standard deviation (σ) of 316 nm for the Gaussian profile.

Once the laser was configured with the parameters previously mentioned, the next step consists in applying different sets of powers to the different samples, since each sample has a different density, a different heat capacity, and different types of coating, the power had to be adjusted to accurately calculate the thermal conductivity of each sample.

The simulations in this section show the different thermal conductivity obtained for each

of the samples. These results successfully match with the experimental data obtained from Raman spectroscopy, also detailed in this work.

2.5 Temperature Calibration

To use Raman thermometry, it is crucial to calibrate the peak positions of the different materials under test. For the purpose of the following experiments, we first used a piece of bulk silicon to calibrate the peak shift at different temperatures.

To perform the experiment, we placed the piece of material in an environmental stage. The bottom of the substrate is in contact with a thermal control chuck that is heated to a specific temperature. After a period of equalization time, we can assume that the substrate has reached the temperature of the stage. We then use a low laser power setting on the Raman to obtain a spectrum of the material under test. As shown in Figure 2.6, the Si substrate peak shifts with respect to the temperature of the chuck.

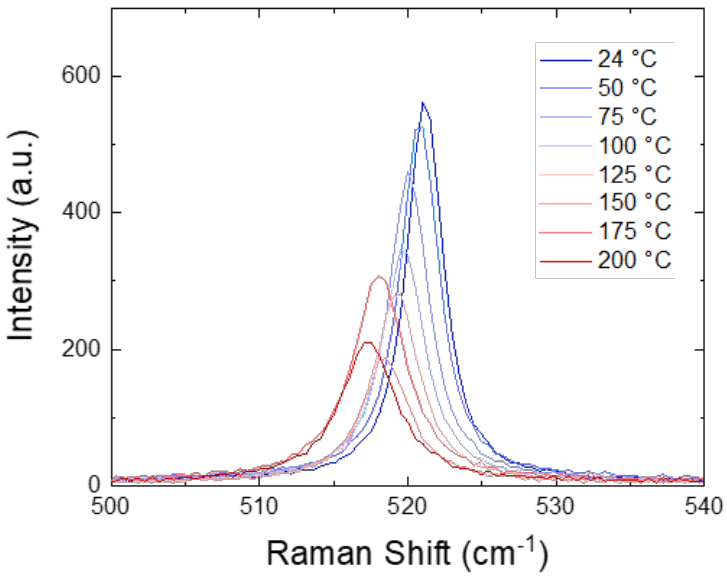

Figure 2.5: Si peak position and intensity data. The peak position and intensity varies with respect to the temperature.

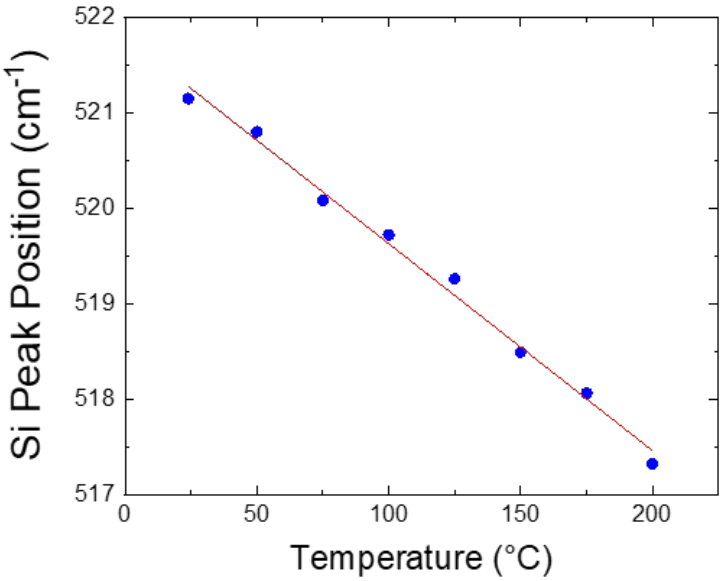

Figure 2.6: Si Peak shifts linearly with respect to the temperature.

Our experimental data (Fig. 2.6) shows that Si peak position shifts as a linear function of the temperature. The shift rate is measured at 0.02 $cm^{-1}/^{\circ}C$, consistant with measurements from previous literature [20].

We performed a similar calibration on graphene on a silicon substrate. The sample is prepared by using commercially available graphene grown on copper. A layer of PMMA is coated on top of the graphene for ease of transfer. The copper is then etched away using a ferric chloride solution. The graphene and PMMA layer left over floating on the solution is cleaned in de-ionized water and physically transferred onto the silicon substrate. A similar experiment is then performed on the graphene layer.

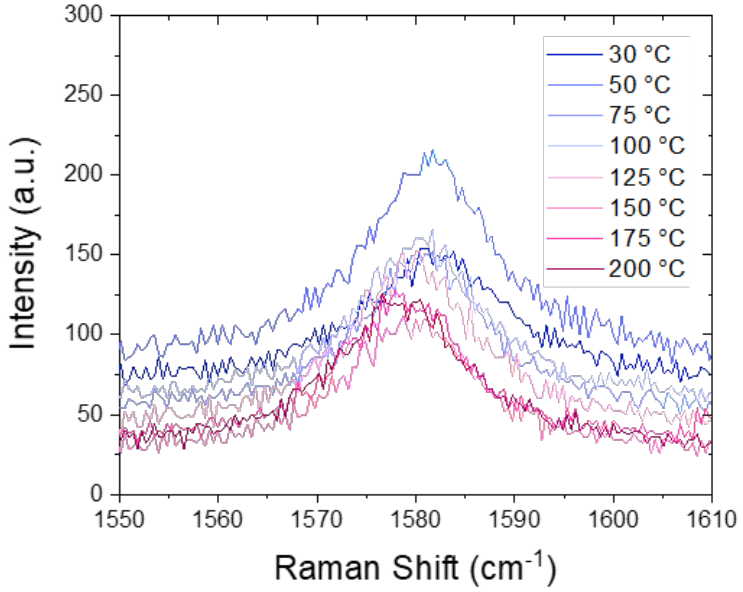

Figure 2.7: Graphene peak shifts similar to the silicon peak. Due to the fact that the material is a single layer of atoms, the signals are weaker than that of the silicon substrate.

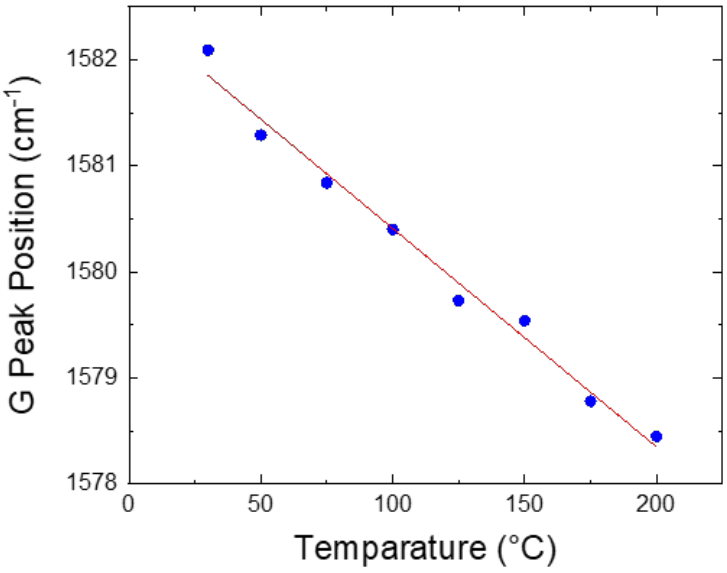

Figure 2.8: Graphene peak shift vs. temperature

The graphene peak shifts at 0.02 $cm^{-1}/^{\circ}C$ consistent with measurements from previous experiments [21].

A Laser Heating Experiment is then performed to extract the thermal conductivity of bulk Si. The raman laser characterized in the previous chapters is used to measure the thermal conductivity of Si substrate.

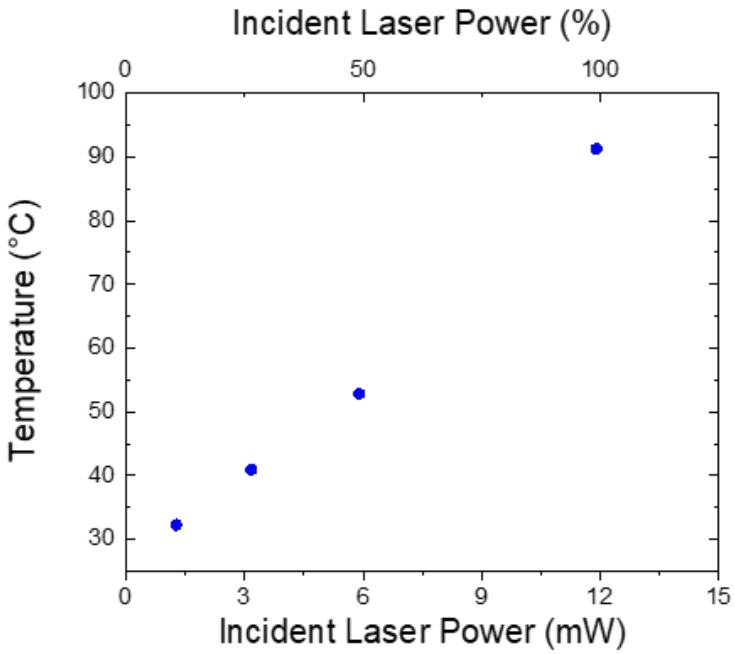

Figure 2.9: Silicon laser heating

With the information from the temperature calibration and power calibration, we can obtain the information plotted in Figure 2.9. By plugging the information and adjusting only the thermal conductivity, we can extract the parameter with fair confidence.

(a) FEA model surface view (b) FEA model crossection

Figure 2.10: FEA model of Si laser heating experiment

The extracted silicon thermal conductivity is 130 W/mK which fits previous work using other methods [22].

Chapter 3

Experimental Investigation

3.1 Overview

The experimental methods we applied in this investigation involved the Raman thermometry methods mentioned in the previous chapter. Traditionally samples are measured using methods that involve a controlled heat flux and a temperature readout [23]. The basic idea is a heat flux introduced to a material creates a change in temperature. Heat flux is described as the change in energy per area, and heat conductivity is how well the material conducts heat. This is being described as an analog of Ohm's law [24], with the reciprocal of the thermal conductivity being the thermal resistance.

$$\nabla T = \frac{\left(\dot{Q}/A\right)}{\kappa} \tag{3.1}$$

The traditional methods have limitations for thin films as they are most suited for bulk materials. Applying a heat flux and measuring changes in temperature often requires physically attaching the materials onto a large apparatus [23]. It requires the material to have structural integrity and a large enough sample to work with. With the new graphene based materials this is simply not possible. Any attempt to deposit or mechanically attach thermometers and heaters will obliterate the delicate structure of graphene, as discussed in the later parts of this work. In this work, we use the technique Raman thermometry to characterize the thermal characteristics of the materials. Raman thermometry has the advantage that it is a none destructive method to characterize the material. As discussed in the previous chapter, we have characterized the laser power and the spot size of the laser for specific objectives on the Raman spectroscopy apparatus. We have used that data to determine the $\dot{Q}/A$ of equation 3.1. Also we used the peak shift data captured from the Raman acquisition

to determine the change in temperature at the laser spot at the same time. We will then fit the data back to the FEA model for thermal conductivity(κ) extraction.

3.2 Free Standing Graphene Foam

The free standing graphene foam is a commercially available material. It is likely grown on a metal with foam like structure by chemical vapor deposition methods.

3.2.1 Optical Characterization

The material is observed in low and high magnification under the microscope in the center and edge. See Figure 3.1, the foam is physically very delicate and can easily be broken into pieces by any kind of force.

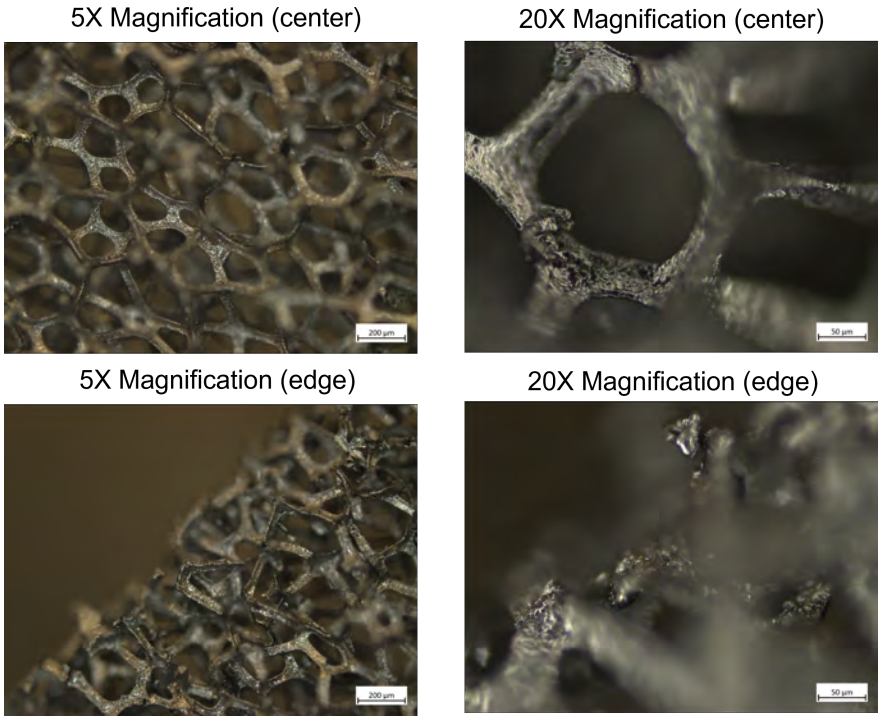

Figure 3.1: Optical images of free standing graphene foam.

3.2.2 Raman Spectra

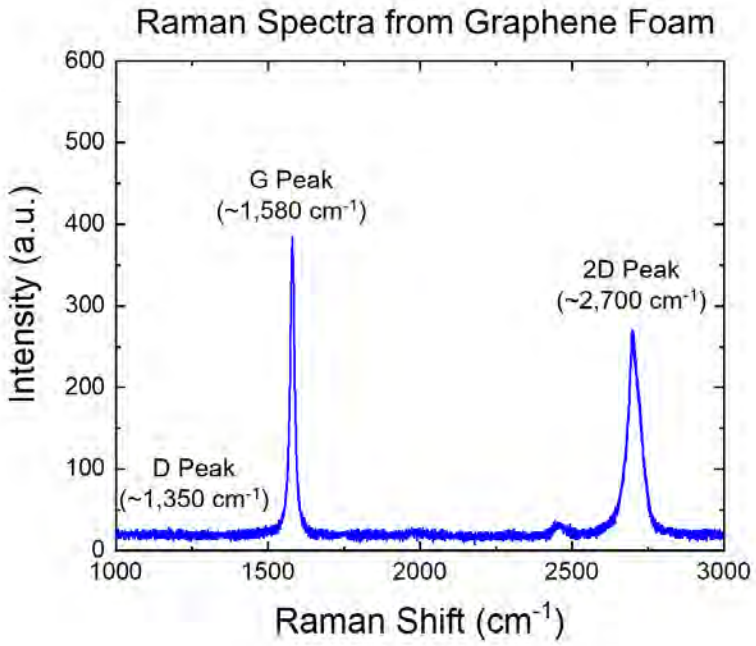

Figure 3.2: Raman spectra of free standing graphene foam

The peak at 1350 cm^{-1} is the D peak which provides information on the quality of the material [25]. It will rise in intensity due to defects in the material. The G Peak at 1580 cm^{-1} provides information on temperature [21]. As characterized in the previous chapter, the G peak shifts in a very linear way according to the temperature of the material. The 2D peak at 2700 cm^{-1} changes shape and shifts due to the layers present in the material. In this case, we can see that the material is of relative high quality. The 2D peak shows broadening and that is due to the material is not a single layer of graphene.

3.2.3 Heating Data

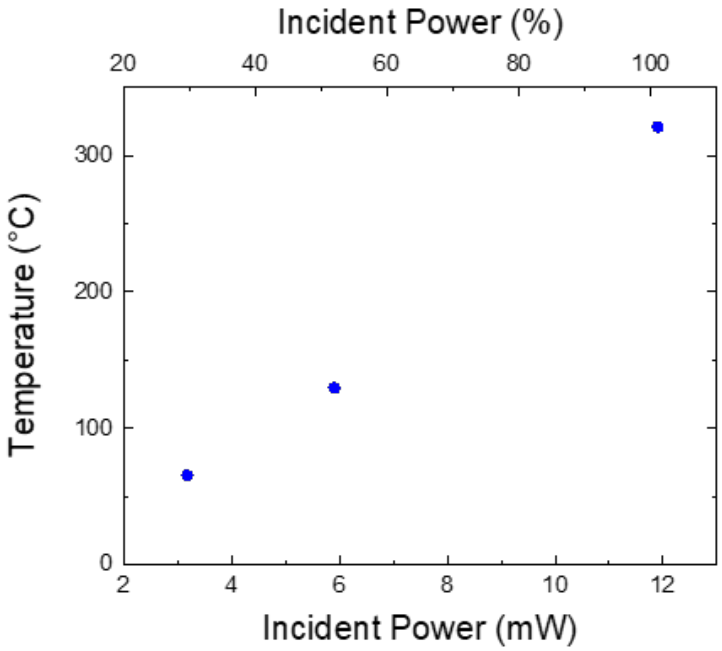

Figure 3.3: Heating data of free standing graphene foam

By varying the laser power, we are able to get the heating data shown in Fig.3.3. By inserting the data into the FEA model shown in the previous chapter, we are able to extract the thermal conductivity of the free standing graphene foam to be 1.9W/mK. Which matches well with data that has been reported [14].

3.2.4 Au Sputtering

One of the free standing graphene foam samples was prepared with gold sputtered on the top surface. We did not observe a substancial difference under the optical microscope. However, the Raman spectra shown in Fugure 3.4, a substancial difference in material quality. The D peak, which is indicative of the defects in the material has risen to 175 counts [25]. The G peak changed in shape and the 2D peak is very weak compared to the previous

sample. The gold is not thick enough to reflect or absorb all the laser light and Raman signal, but the process of sputtering has damaged the material enough for the Raman signal to deteriorate.

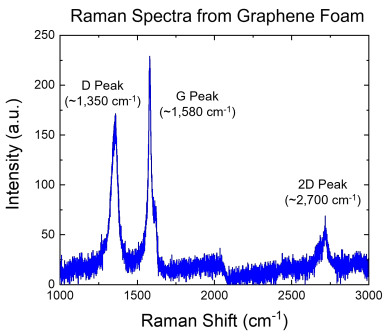

(a) Au sputtered graphene foam Raman spectra

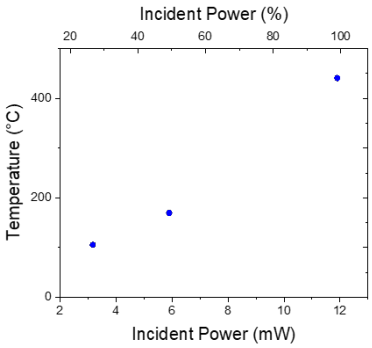

(b) Au sputtered graphene foam heating data

Figure 3.4: Au sputtered graphene Raman and laser heating experiment

Fig. 3.4 shows the heating data of the sputtered material. We can observe that the material was heated to a much higher temperature with similar heat flux. The extrapolated $\kappa_{foam} = 1.42$ W/mK is lower than that of the defect free material.

3.3 Graphene-Nickel Foam

A similar material we also characterized is graphene grown on nickel foam. The material is much more robust and rigid compared to the free standing graphene foam.

3.3.1 Optical Characterization

From Fig. 3.5 we can see that visually it is very similar to the free standing foam but does have a silver matellic sheen to it.

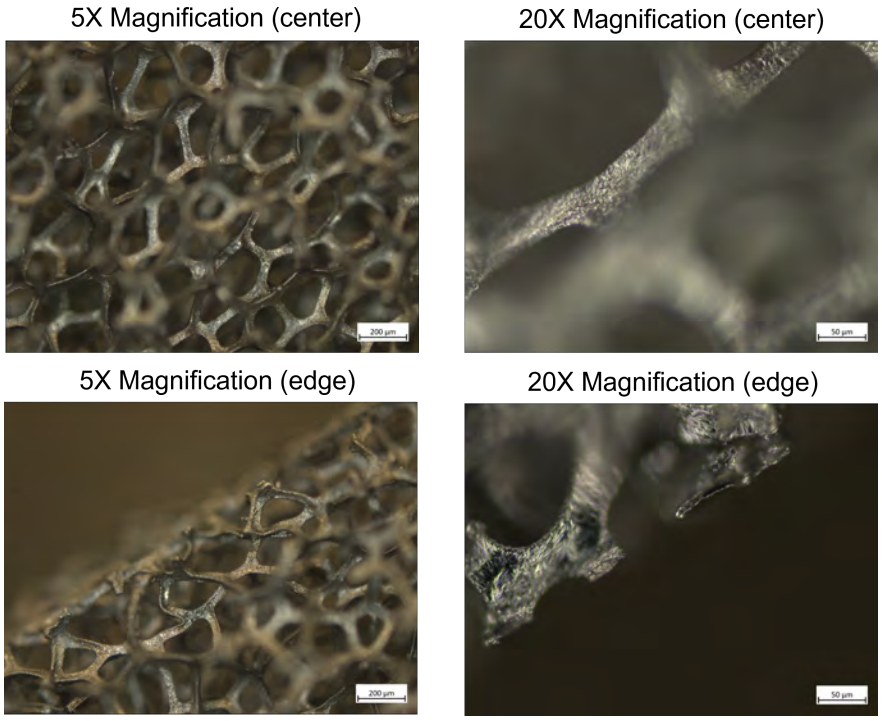

Figure 3.5: Optical images of Graphene-Ni foam.

3.3.2 Raman Spectra

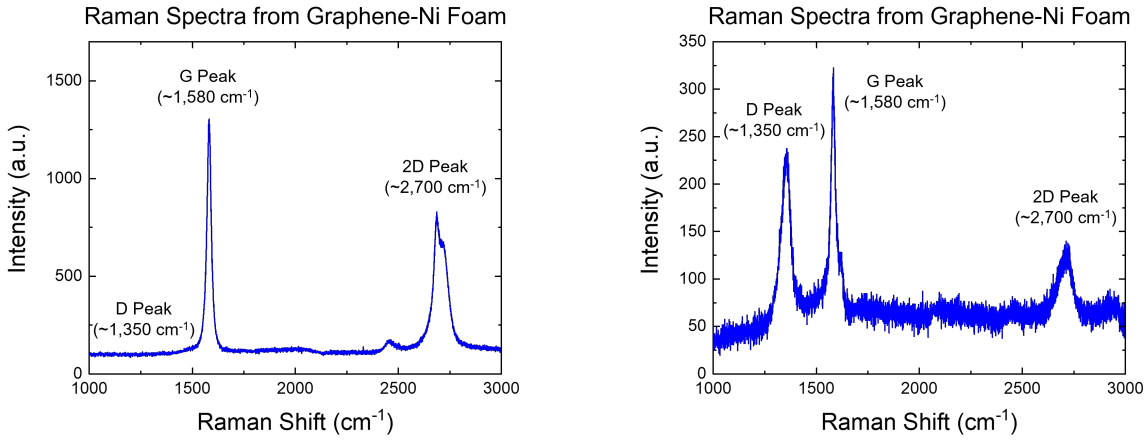

(a) Raman spectra of Graphene-Ni foam

(b) Au sputtered Graphene-Ni foam

Figure 3.6: Raman Spectra of Graphene-Ni foam and Au sputtered Graphene-Ni Foam

In Fig. 3.6 we can clearly see the difference between the quality of materials. The sputtering introduced many defects in the material. The defect peak has risen to a comparable height as the G peak [25]. The 2D peak shows that before sputtering, the graphene is of reasonable quality, but is not single crystalline.

3.3.3 Heating Data

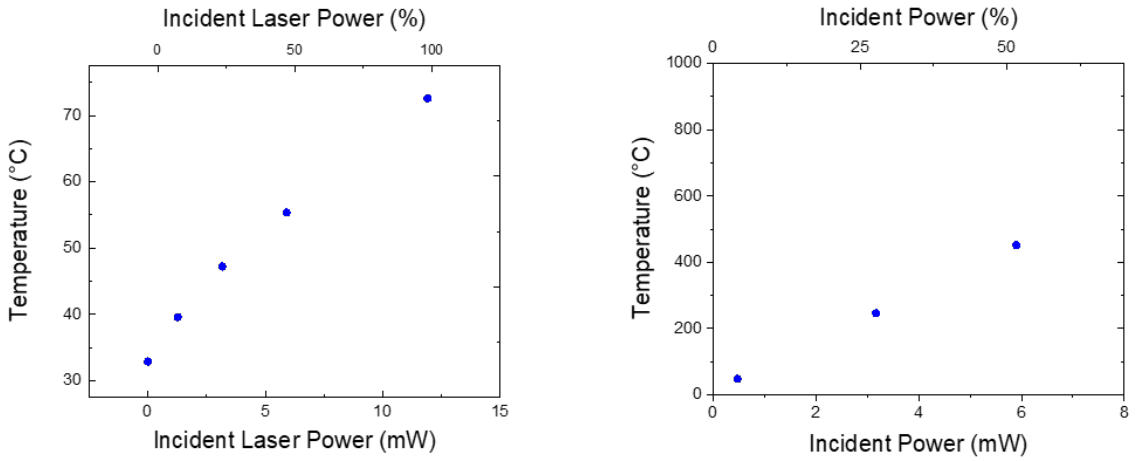

(a) Heating data of the Graphene-Ni Foam

(b) Heating data of the Au sputtered Graphene-Ni Foam

Figure 3.7: Raman thermometry of Graphene-Ni foam and Au sputtered Graphene-Ni Foam

From the heating data, we can see that the Graphene-Ni foam does not heat up much compared to the previous heating data. But in contrast the sputtered sample exerienced much more heating. The extracted thermal conductivity of the Graphene-Ni foam is 26.2 W/mK, and for the sputtered sample 2.56 W/mK.

3.4 Graphene-Cu Foam

Graphene-Cu foam is a material that we also tested. Compared to nickel, it is a denser material and in theory should produce similar results.

3.4.1 Optical Characterization

We visually characterized the copper foam. It is similar to all the other foams but copper is clearly visible from the microscope.

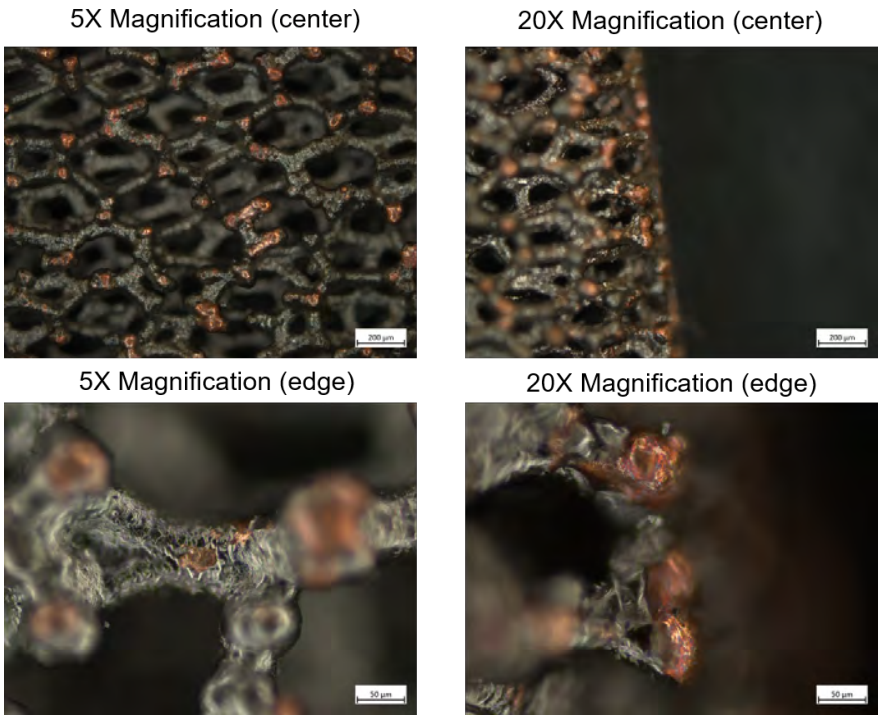

Figure 3.8: Optical images of Graphene-Cu foam.

3.4.2 Raman Spectra

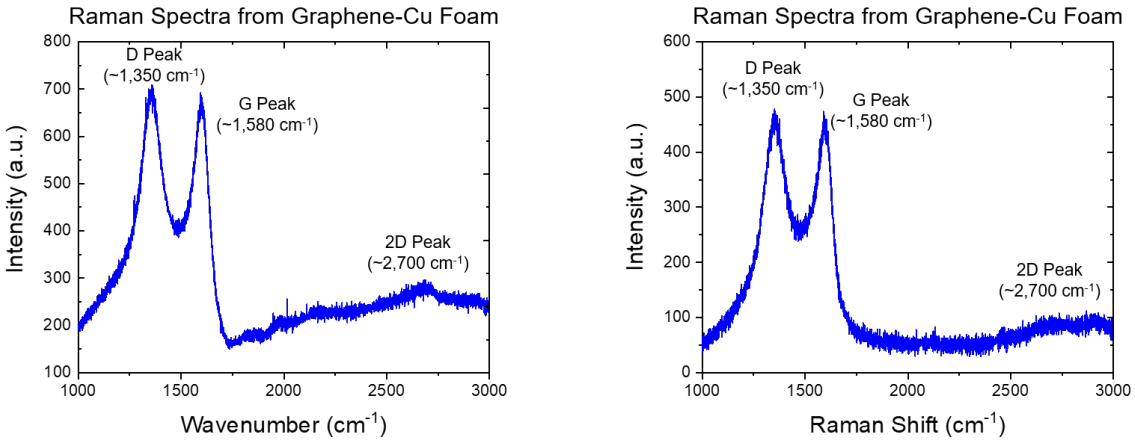

(a) Raman spectra of Graphene-Cu foam

(b) Au sputtered Graphene-Cu foam

Figure 3.9: Raman spectra of Graphene-Cu foam and Au sputtered Graphene-Cu foam

The Cu foam exhibits a clear defect peak(D) and broadening of the G peak. This is indicative of the material being very low quality. The intensity is also very low for the 2D peak.

3.4.3 Heating Data

The measured temperature of the laser heating experiment is relatively unstable compared to the previous foams.

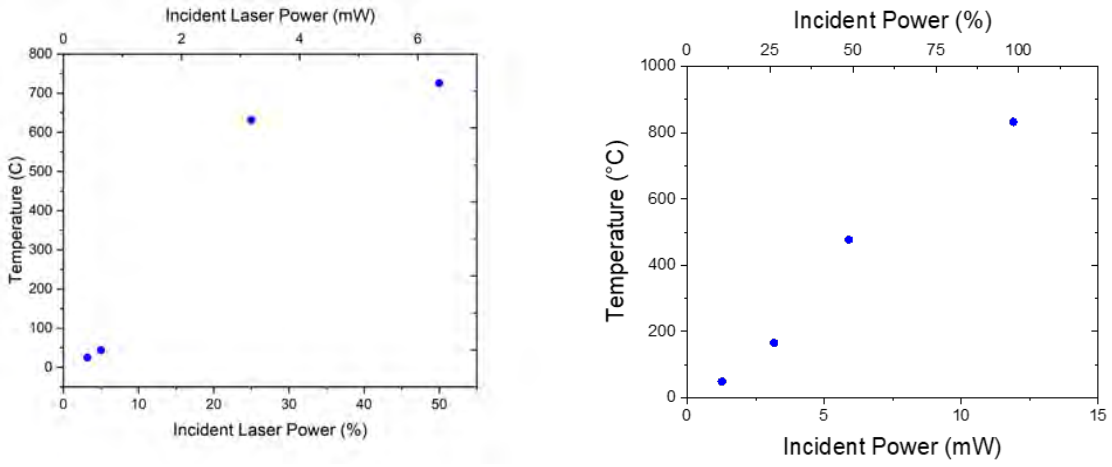

(a) Heating data of the Graphene-Cu foam

(b) Heating data of the Au sputtered Graphene-Cu foam

Figure 3.10: Raman thermometry of Graphene-Cu foam and Au sputtered Graphene-Cu foam

The extracted thermal conductivity of the Graphene-Cu foam is 1.09 W/mK. The extracted thermal conductivity of the sputtered foam is 1.51 W/mK. Compared to other works our numbers are relativly low. This is probably because of the relative low quality of the material [26].

3.5 Graphene Film Paper

The graphene film paper is a commercially available material that resembles the looks of a sheet of paper.

3.5.1 Optical Characterization

Visually it is very smooth and has a very low density, measured to be 1.25 g/cm^3.

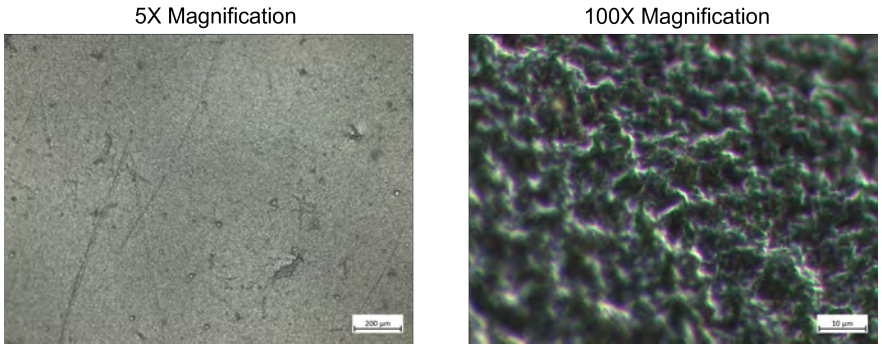

Figure 3.11: Optical images of graphene film paper.

3.5.2 Raman Spectra

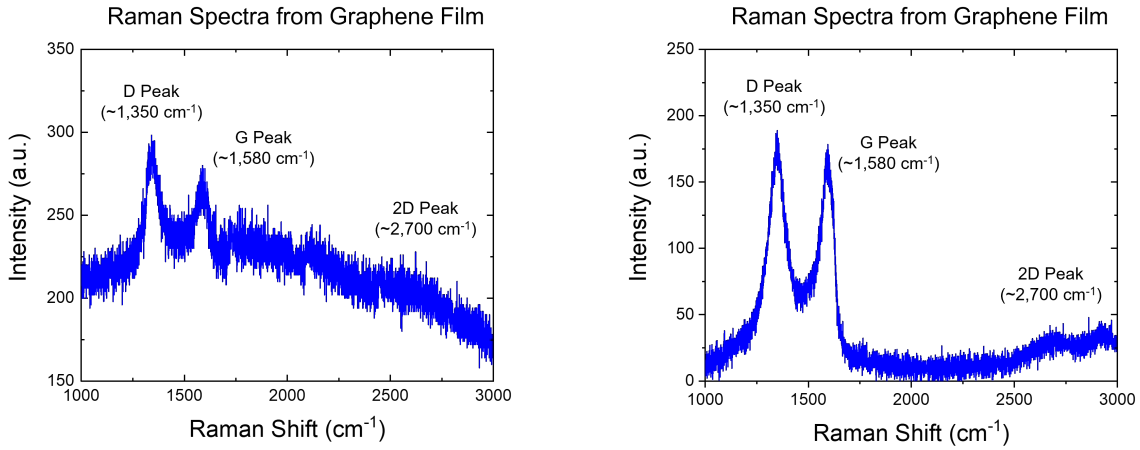

(a) Raman spectra of graphene film

(b) Au sputtered graphene film

Figure 3.12: Raman spectra of graphene film paper and Au sputtered graphene film paper

The graphene film paper exhibits very characteristics of very low quality. It does not have a distinguishable 2D peak. The D peak and the G peak in the material has morphed together to a large twin hump that resembles graphene oxide [27].

3.5.3 Heating Data

The measured temperature of the laser heating experiment is extremely high. The experiment actually resulted in burning a hole in the material. This is an indication of an extremely low quality material and has very low thermal conductivity.

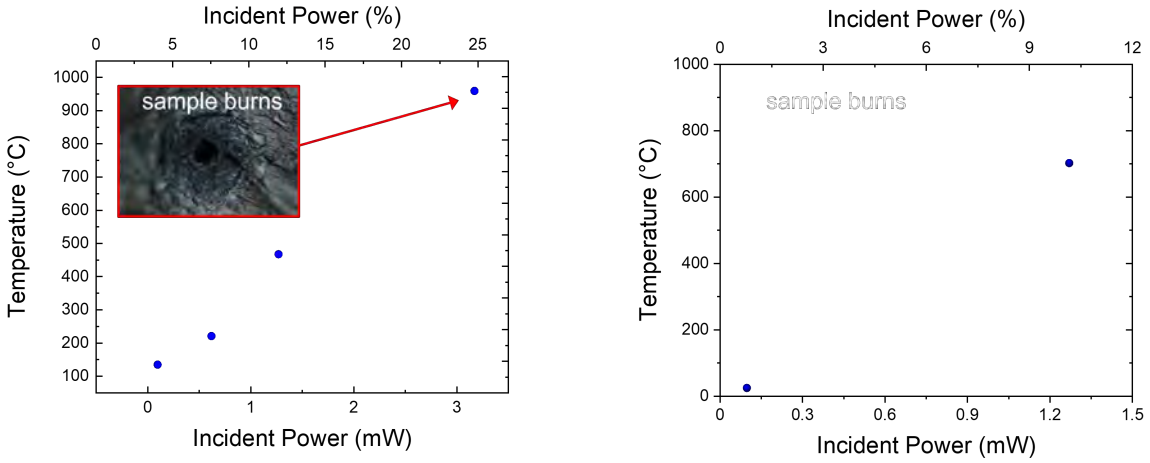

(a) Heating data of the graphene film paper

(b) Heating data of the Au sputtered graphene paper film

Figure 3.13: Raman Thermometry of graphene film paper and Au sputtered graphene film paper

The extracted thermal conductivity of the graphene paper film is 0.898W/ mK. The extracted thermal conductivity of the sputtered paper is 0.49 W/mK. This matches well with other works. We think the material is anisotropic material resulting in low cross-plane thermal conductivity [4].

Chapter 4

Conclusions and Future Work

Raman thermometry is a very powerful tool and allowed us to conduct the experiments on these irregularly shaped materials. Through the experiments we have obtained the data shown in the table below. Because most of the materials presented in this work contain a large portion of air, we can calculate the thermal conductivity of the solid using volume loading factor [14]. The results we obtained are comparable with the data depicted in other

Table 4.1: Thermal Conductivity of Graphene Based Materials

Material	Density (g/cm^3)	Quality	κ_{bulk} (W/mK)	κ_{solid}(W/mK)
FSG	0.0202	High	1.9	630
Au FSG	0.0202	Low	1.42	415
G-Ni	0.314	High	26.2	501
Au G-Ni	0.314	Low	2.56	250
G-Cu	0.332	Low	1.09	125
Au G-Cu	0.332	Low	1.51	125
G-Film	1.25	Low	0.898	0.898
Au G-Film	1.25	Low	0.49	0.49

work [14]. We measured high thermal conductivity in the solid portion of the higher quality graphene materials but it is limited by the volume fraction. Since air makes up a large portion of the material, the overall bulk thermal conductivity appears to be low.

The bombardment of energetic particles through the process of sputtering has shown very clear damage to the graphene layers [28]. The gold sputtered samples consistently exhibit

characteristics of lower quality. The quality of material is seen to have a large impact on the thermal conductivity of the material. The higher quality free standing graphene foam and Graphene-Nickel foam exhibits better thermal conductivity characteristics compared to the Graphene-Copper foam. The lower quality of the sputtered materials also lead to lower thermal conductivity.

Our future work will involve more carbon based materials. Since the solid thermal conductivity of the materials investigated in this paper shows promising properties, we will be looking into improving the properties of these materials. A large portion of the thermal conductivity is dominated by the volume loading fraction. We will be looking into increasing the carbon and reducing the air content. There is also room to improve the material quality. We have found that the material quality has a profound impact on the thermal conductivity of carbon based materials. Better material quality will lead to better thermal conductivity.

BIBLIOGRAPHY

[1] S. Salahuddin, K. Ni, and S. Datta, "The era of hyper-scaling in electronics," *Nature Electronics*, vol. 1, no. 8, p. 442–450, 2018. 1

[2] A. Ward, D. A. Broido, D. A. Stewart, and G. Deinzer, "Ab initio theory of the lattice thermal conductivity in diamond," *Physical Review B*, vol. 80, no. 12, 2009. 1

[3] A. A. Balandin, S. Ghosh, W. Bao, I. Calizo, D. Teweldebrhan, F. Miao, and C. N. Lau, "Superior thermal conductivity of single-layer graphene," *Nano letters*, vol. 8, no. 3, pp. 902–907, 2008. 1

[4] A. Alofi and G. P. Srivastava, "Thermal conductivity of graphene and graphite," *Physical Review B*, vol. 87, no. 11, 2013. 1, 25

[5] J. H. Seol, I. Jo, A. L. Moore, L. Lindsay, Z. H. Aitken, M. T. Pettes, X. Li, Z. Yao, R. Huang, D. Broido, N. Mingo, R. S. Ruoff, and L. Shi, "Two-dimensional phonon transport in supported graphene," *Science*, vol. 328, no. 5975, pp. 213–216, 2010. [Online]. Available: https://www.science.org/doi/abs/10.1126/science.1184014 2

[6] B. Amorim and F. Guinea, "Flexural mode of graphene on a substrate," *Physical Review B*, vol. 88, no. 11, 2013. 2

[7] Z.-Y. Ong, B. Qiu, S. Xu, X. Ruan, and E. Pop, "Flexural resonance mechanism of thermal transport across graphene-sio2 interfaces," *Journal of Applied Physics*, vol. 123, no. 11, p. 115107, 2018. 2

[8] E. Pop, V. Varshney, and A. K. Roy, "Thermal properties of graphene: Fundamentals and applications," *MRS bulletin*, vol. 37, no. 12, pp. 1273–1281, 2012. 2

[9] S. Vaziri, E. Yalon, M. Muñoz Rojo, S. V. Suryavanshi, H. Zhang, C. J. McClellan, C. S. Bailey, K. K. Smithe, A. J. Gabourie, V. Chen *et al.*, "Ultrahigh thermal isolation across heterogeneously layered two-dimensional materials," *Science advances*, vol. 5, no. 8, p. eaax1325, 2019. 2

[10] C. Chiritescu, D. G. Cahill, N. Nguyen, D. Johnson, A. Bodapati, P. Keblinski, and P. Zschack, "Ultralow thermal conductivity in disordered, layered wse2 crystals," *Science*, vol. 315, no. 5810, pp. 351–353, 2007. 2

[11] H. Kim, A. A. Abdala, and C. W. Macosko, "Graphene/polymer nanocomposites," *Macromolecules*, vol. 43, no. 16, pp. 6515–6530, 2010. 2

[12] A. Reina, X. Jia, J. Ho, D. Nezich, H. Son, V. Bulovic, M. S. Dresselhaus, and J. Kong, "Large area, few-layer graphene films on arbitrary substrates by chemical vapor deposition," *Nano letters*, vol. 9, no. 1, pp. 30–35, 2009. 2

[13] X. Li, W. Cai, J. An, S. Kim, J. Nah, D. Yang, R. Piner, A. Velamakanni, I. Jung, E. Tutuc *et al.*, "Large-area synthesis of high-quality and uniform graphene films on copper foils," *science*, vol. 324, no. 5932, pp. 1312–1314, 2009. 2

[14] M. T. Pettes, H. Ji, R. S. Ruoff, and L. Shi, "Thermal transport in three-dimensional foam architectures of few-layer graphene and ultrathin graphite," *Nano Letters*, vol. 12, no. 6, p. 2959–2964, 2012. 2, 17, 26

[15] S. Périchon, V. Lysenko, B. Remaki, D. Barbier, and B. Champagnon, "Measurement of porous silicon thermal conductivity by micro-raman scattering," *Journal of Applied Physics*, vol. 86, no. 8, pp. 4700–4702, 1999. [Online]. Available: https://doi.org/10.1063/1.371424 2, 4

[16] 2022. [Online]. Available: https://www.thorlabs.com/newgrouppage9.cfm?objectgroup_id=3422 4

[17] M. Mauck, "Knife-edge profiling of q-switched nd:yag laser beam and waist," *Appl. Opt.*, vol. 18, no. 5, pp. 599–600, Mar 1979. [Online]. Available: http://opg.optica.org/ao/abstract.cfm?URI=ao-18-5-599 5

[18] W. Cai, A. L. Moore, Y. Zhu, X. Li, S. Chen, L. Shi, and R. S. Ruoff, "Thermal transport in suspended and supported monolayer graphene grown by chemical vapor deposition," *Nano Letters*, vol. 10, no. 5, p. 1645–1651, 2010. 6

[19] E. Yalon, O. B. Aslan, K. K. Smithe, C. J. McClellan, S. V. Suryavanshi, F. Xiong, A. Sood, C. M. Neumann, X. Xu, K. E. Goodson, and et al., "Temperature-dependent thermal boundary conductance of monolayer mos2 by raman thermometry," *ACS Applied Materials & Interfaces*, vol. 9, no. 49, p. 43013–43020, 2017. 6

[20] T. R. Hart, R. L. Aggarwal, and B. Lax, "Temperature dependence of raman scattering in silicon," *Physical Review B*, vol. 1, no. 2, p. 638–642, 1970. 10

[21] I. Calizo, A. A. Balandin, W. Bao, F. Miao, and C. N. Lau, "Temperature dependence of the raman spectra of graphene and graphene multilayers," *Nano Letters*, vol. 7, no. 9, p. 2645–2649, 2007. 12, 16

[22] C. J. Glassbrenner and G. A. Slack, "Thermal conductivity of silicon and germanium from 3°k to the melting point," *Physical Review*, vol. 134, no. 4A, 1964. 13

[23] H. Czichos, T. Saito, and L. Smith, *Springer Handbook of Materials Measurement Methods*. Springer, 2007. 14

[24] E. T. Swartz, "Solid-solid thermal boundary resistance," Ph.D. dissertation, UMI Dissertation Services, 1987. 14

[25] A. C. Ferrari, J. C. Meyer, V. Scardaci, C. Casiraghi, M. Lazzeri, F. Mauri, S. Piscanec, D. Jiang, K. S. Novoselov, S. Roth, and et al., "Raman spectrum of graphene and graphene layers," *Physical Review Letters*, vol. 97, no. 18, 2006. 16, 17, 20

[26] K. Chan, C. Tso, A. Hussain, and C. Y. Chao, "A theoretical model for the effective thermal conductivity of graphene coated metal foams," *Applied Thermal Engineering*, vol. 161, p. 114112, 2019. 23

[27] D. López-Díaz, M. López Holgado, J. L. García-Fierro, and M. M. Velázquez, "Evolution of the raman spectrum with the chemical composition of graphene oxide," *The Journal of Physical Chemistry C*, vol. 121, no. 37, p. 20489–20497, 2017. 24

[28] N. Pliatsikas, O. Karabinaki, M. Zarshenas, G. Almyras, I. Shtepliuk, R. Yakimova, J. Arvanitidis, D. Christofilos, and K. Sarakinos, "Energetic bombardment and defect generation during magnetron-sputter-deposition of metal layers on graphene," *Applied Surface Science*, vol. 566, p. 150661, 2021. 26

[29] M. T. Pettes, H. Ji, R. S. Ruoff, and L. Shi, "Thermal transport in three-dimensional foam architectures of few-layer graphene and ultrathin graphite," *Nano letters*, vol. 12, no. 6, pp. 2959–2964, 2012.